19.9%-efficient ultrathin solar cell based on a 205nm-thick GaAs absorber and a silver nanostructured back mirror

Hung-Ling Chen[1], Andrea Cattoni[1], Romaric De Lépinau[1,2], Alexandre W. Walker[3,5], Oliver Hoehn[3], David Lackner[3], Gerald Siefer[3], Marco Faustini[4], Nicolas Vandamme[1], Julie Goffard[1,2], Benoît Behaghel[1], Christophe Dupuis[1], Nathalie Bardou[1], Frank Dimroth[3], Stéphane Collin[1,2*]

[1] *Centre for Nanoscience and Nanotechnology (C2N), CNRS, University Paris-Sud / Paris-Saclay, 91120 Palaiseau, France*

[2] *Institut Photovoltaïque d'Ile-de-France (IPVF) – 91120 Palaiseau, France*

[3] *Fraunhofer Institute for Solar Energy Systems (ISE), 79110 Freiburg, Germany*

[4] *Sorbonne Université, UPMC Univ Paris 06, CNRS, Collège de France, Chimie de la Matière Condensée de Paris, 75005 Paris, France*

[5] *Present address: National Research Council of Canada, Ottawa, Ontario K1A 0R6, Canada*

**email: stephane.collin@c2n.upsaclay.fr*

Abstract

Conventional photovoltaic devices are currently made of relatively thick semiconductor layers, about 150 µm for silicon, and 2–4 µm for CIGS, CdTe or III-V direct bandgap semiconductors. Ultrathin solar cells using 10 times thinner absorbers could lead to considerable material and processing time savings. Theoretical models suggest that light trapping can compensate for the reduced single-pass absorption, but optical and electrical losses have greatly limited the performances of previous attempts. Here, we propose a strategy based on multi-resonant absorption in planar active layers, and we report a 205 nm-thick GaAs solar cell with a certified 19.9% efficiency. It uses a nanostructured silver back mirror fabricated by soft nanoimprint lithography. Broadband light trapping is achieved with multiple overlapping resonances induced by the grating and identified as Fabry-Perot and guided-mode resonances. A comprehensive optical and electrical analysis of the complete solar cell architecture provides the pathway for further improvements and shows that 25% efficiency is a realistic short-term target.

1. Introduction

The efficiency of single-junction solar cells has improved consistently over time for both crystalline silicon (c-Si) and thin-film (CIGS, CdTe, GaAs) technologies, and contributed to the cost decrease and widespread development of photovoltaic devices. To date, solar cells made of c-Si reach 26.7% photoconversion efficiency using 165 µm-thick Si wafers (1). With high optical absorption and radiative efficiency, GaAs approaches the Shockley-Queisser limit (2) and reached a record efficiency of 29.1% with 1–2µm-thick single-junction solar cells (3,4). On the other hand, theoretical light-trapping models suggest that the solar cell thickness can be reduced by more than one order of magnitude while preserving state-of-the-art short-circuit currents (5,6). Such a thickness reduction improves the industrial throughput and saves scarce materials (e.g. tellurium in CdTe, indium in CIGS and III-V). It also helps improve the performance of solar cells. For a given density of defects, non-radiative bulk recombination decreases with the thickness, allowing for the use of materials with a reduced diffusion length. For space applications, ultrathin GaAs cells show increased tolerance to high-energy particle bombardment (7). Overall, thinning the absorber has a beneficial effect on both charge carrier collection and open-circuit voltage. The best solar cell would be an ultrathin solar cell if maximal absorption can be maintained through efficient light trapping.

Different light trapping strategies have been proposed and successfully employed to compensate for the short- circuit current drop due to incomplete absorption in ultrathin layers (8 9,10). Disordered nanotextures are a conventional approach and allowed 8.6% efficiency with only 830nm-thick silicon layers (11). Front surface nanotexturing with inverted pyramid arrays coupled with a highly reflective back mirror were optimized for ultrathin silicon solar cells (12,13,14) and led to 15.4% efficiency with 10µm-thick c-Si layers (12). However, efficiencies exceeding 20% were only achieved with c-Si solar cells thicker than 40µm (15). Nanostructured back mirrors were used to increase long-wavelength absorption in III-V/Si tandem solar cells (16), and a numerical study has shown broadband absorption capabilities in 150nm-thick CIGS solar cells (17). Dielectric nanoparticles were also successfully introduced at the rear side of CIGS solar cells with no significant impact on FF and V_{oc}, leading to 12.3% efficiency with a thickness of 460nm (18). On the contrary, a-Si:H deposited on textured substrate shows improved absorption (19, 20) but low electrical performances. Overall, the best light trapping designs tend to avoid texturation of the absorber.

Ultrathin GaAs solar cells can be considered as a model system to investigate the potential of light-trapping for high-efficiency ultrathin solar cells. Metal nanoparticles (21,22) and nanogrids (23) can improve absorption via plasmonic resonances (24), but the beneficial effect is usually compensated by metal absorption losses at short wavelengths. The integration of a highly reflective back mirror is a first requirement for efficient light trapping (25), and it can boost the open-circuit voltage (V_{oc}) through the photon recycling effect (26,27,28). Yang et al. have used a rough scattering Au back-mirror to further enhance light trapping. They achieved 19.1% efficiency with 300nm-thick solar cells (29). In contrast, Lee et al. combined front-side periodic TiO_2 nanostructures with a flat back reflector and reached 16.2% efficiency in 200nm-thick GaAs solar cells (30). State-of-the-art ultrathin GaAs solar cells are listed in Table 1. Overall, previous achievements make use of light scattering and diffraction and lie below numerical predictions for double-pass absorption.

In this work, we propose a light trapping strategy based on multi-resonant absorption. We demonstrate a certified efficiency of 19.9% with a 205nm-thick GaAs solar cell using planar active layers and a silver nanostructured back mirror with a periodical pattern. It is fabricated using a low-cost and scalable technique based on direct embossing of TiO_2 sol-gel derived film. The back mirror induces multiple overlapping resonances that provide efficient light trapping over a broad spectral range. The short-circuit current exceeds significantly an ideal double-pass absorption model while preserving FF and Voc. A detailed analysis of the optical and electrical properties of the device shows the path to reach 25% conversion efficiency using the same light-trapping scheme.

Table 1: Comparison of record thin and ultrathin single-junction GaAs solar cell performances with different absorber thicknesses. J_{sc} values are normalized by the result of an ideal double-pass absorption model ($A = 1 - e^{-2\alpha t}$) to highlight the light trapping capability.

	Absorber thickness *t* (nm)	J_{sc} (mA/cm²)	J_{sc}/double-pass absorption	V_{oc} (V)	FF	Efficiency (%)
Kayes *et al*. (3,4)	≥1000	29.68	0.94	1.122	0.865	29.1
Yang *et al*. (29)	300	24.5	0.94	1.000	0.778	19.1
Lee *et al*. (30)	200	21.96	0.94	0.942	0.78	16.2
This work	**205**	**24.64**	**1.05**	**1.022**	**0.792**	**19.9**

2. Design and fabrication of ultrathin GaAs solar cells

Ultrathin GaAs solar cells require light trapping structures to compensate for the decreased absorber volume. The rationale of the solar cell design is as follows. III-V active layers are kept flat to avoid

electronic degradation induced by increased surfaces. A periodical pattern is used to enhance absorption through multiple guided-mode resonances. The number of resonances increases with the period p, but diffraction losses at shorter wavelengths ($\lambda<p$ at normal incidence) may induce optical losses in the free space. For this reason, the periodic structure is designed at the backside in the form of a nanostructured metallic mirror so that diffraction in free space can only occur after double-pass absorption. For a GaAs thickness of 200 nm, we found the period p=700 nm as a good trade-off to keep negligible diffraction losses and create numerous resonances over the 700–900 nm wavelength range. The nanostructure back mirror is made of silver because it has the highest reflectivity among metals in this spectral range. It is combined with localized Ni/Ge/Au ohmic contacts (surface coverage: 1%) to collect charge carriers with minimal resistive losses (25). The exact geometry of the grating is optimized with numerical computations based on the rigorous coupled-wave analysis (RCWA) method (31,32,33,34) (details in Methods): Ag square nanostructure width d=420 nm (60% of the period), grating height h=120 nm.

The epitaxial stacks were grown by Metalorganic Vapor Phase Epitaxy (MOVPE) on a n-type GaAs substrate in the following sequence: n+GaAs top contact, n-AlInP window layer, 205 nm GaAs absorber, p-AlGaAs back surface field (BSF) and p+GaAs rear contact. Note that the final solar cell structure is reversed compared to the growth order. A detailed description of the III-V semiconductor layers is given in the Supplementary Table 1. Figure 1(a) shows a schematic of solar cell fabrication sequences. Details about the cell fabrication process are reported in the Methods. Step 1 begins with the fabrication of 5×5 µm² Ti/Au localized ohmic contacts on p+GaAs every 50 µm. Uncovered area of p+GaAs is wet-chemically etched to reduce parasitic optical absorption. In step 2, large-area nanostructures are formed using soft nanoimprint lithography (NIL). TiO_2 sol-gel was spin-coated on the sample surface and printed using a PDMS mold. Figure 1(b) shows a SEM image of the nanoimprinted two-dimensional periodic TiO_2 grating. A silver mirror is deposited to cover conformally both ohmic contacts and TiO_2 nanopatterns (step 3). Then, the mirror side of the sample is bonded to a glass host substrate using a flexible polymer, and the GaAs substrate is removed by chemical etching (step 4). Figure 1(c) shows a cross-section SEM image of a similar sample fabricated until this step, showing the TiO_2/Ag back mirror. Subsequently, Ni/Ge/Au front contact grids are fabricated on n+GaAs, and solar cells of 1×1, 2×2 and 3×3 mm² sizes are protected with photolithography mask in the wet-chemical etching for the mesa. MgF_2/Ta_2O_5 78/48 nm double layers anti-reflection coating (DLARC) is deposited (step 5).

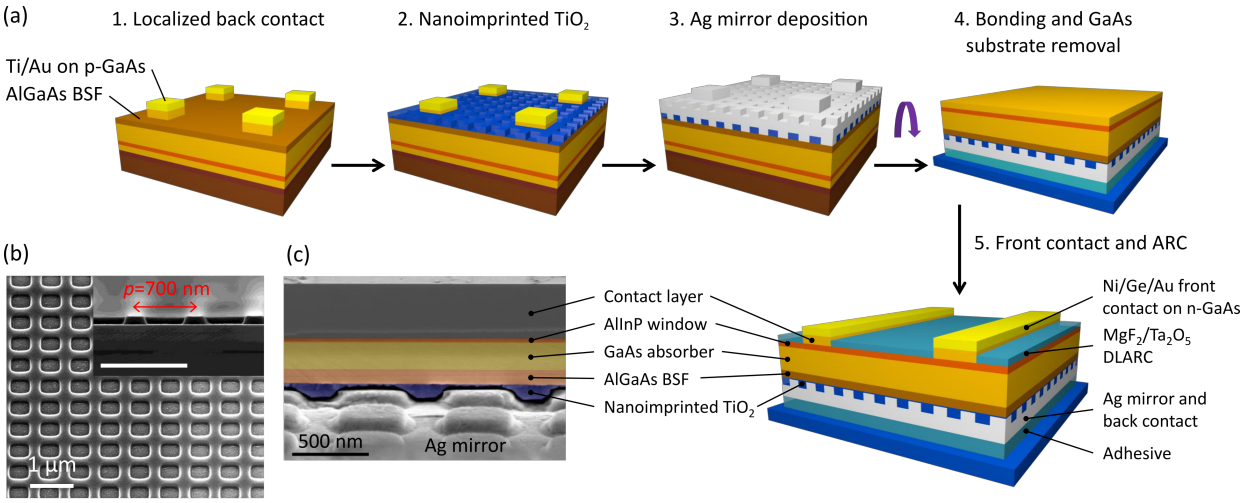

Figure 1: Fabrication process of ultrathin GaAs solar cells with a nanostructured back mirror. (a) Sketches of the main fabrication steps. (b) SEM image of nano-imprinted TiO_2 periodic structures before Ag mirror deposition, the inset shows the cross-section shape of the TiO_2. (c) SEM cross-section view after removing the GaAs substrate, showing the Ag nanostructured back mirror.

3. Performances of ultrathin GaAs solar cells

The best cell was measured by Fraunhofer ISE calibration laboratory under standard test conditions (AM1.5G, 1000 W/m², 25°C, see Supplementary Figures 10-18). The current-voltage (JV) characteristics and external quantum efficiency (EQE) are shown in Figure 2. We achieve a record efficiency of 19.9% using only 205 nm-thick GaAs absorber, with JV parameters: J_{sc}=24.64 mA/cm², V_{oc}=1.022 V and FF=79.2%. The solar cell area is

4.02 mm², which includes front contact grids (~5.5% shading of the total surface) in the calculation of the current density and conversion efficiency. The curve 1-R (R: specular reflectance) plotted in Figure 2(b) represents the total absorption above 700 nm. Its spectral features exhibit multi-resonant absorption and match perfectly with the EQE in the long-wavelength range (700–900 nm). The integral over all photon energies of the EQE with the AM1.5G solar spectrum results in an equivalent J_{sc}=24.39 mA/cm², close to the direct measurement under 1 sun illumination.

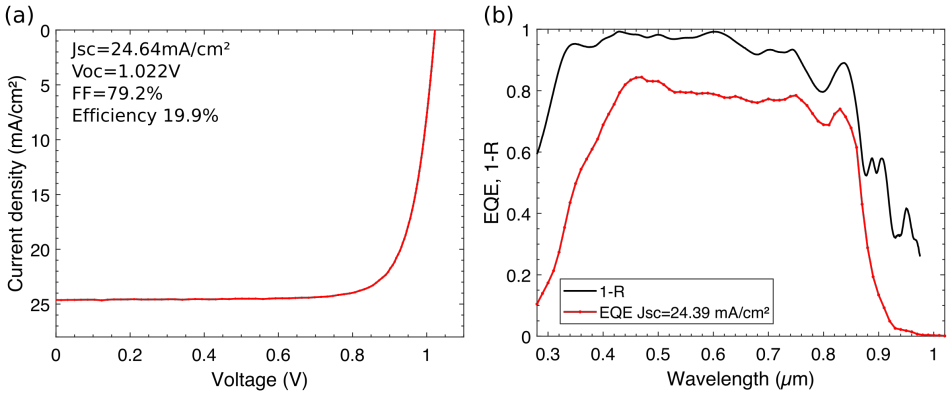

Figure 2: Best ultrathin solar cell based on a 205nm-thick GaAs absorber and a nanostructured Ag mirror. (a) IV characteristics and (b) external quantum efficiency of the 19.9%-efficient solar cell with an aperture area of 4.02 mm² measured at the Fraunhofer ISE calibration laboratory under standard condition (AM1.5G 1000 W/m², 25°C). The black curve 1-R (R: specular reflectance) plotted in (b) exhibits multi-resonant features in agreement with the EQE.

4. Light trapping analysis

To illustrate our light trapping designs, three different solar cells were fabricated out of the same epitaxially grown semiconductor stack: solar cells (A) as-grown on GaAs substrate with a single-layer ARC (70 nm-thick SiN_x), (B) with a flat silver mirror and DLARC, and (C) with a nanostructured silver mirror and DLARC. Their current-voltage characteristics are compared in the Supplementary Figure 1. Their EQE are measured using a Fourier Transform Photocurrent Spectroscopy (FTPS) setup calibrated with a silicon reference cell, and a microscope objective is used to focus light onto a small spot (diameter: a few 100 µm) between the wires of the front contacts in order to avoid shading. The results are plotted in Figure 3(a) and compared to absorption calculations shown in Figure 3(b). The RCWA method is used to compute the electromagnetic fields and absorption spectra in each layer of the solar cell structures. The simulations are in good agreement with EQE measurements (see also Supplementary Note 4) and show a similar trend for the different structures. The light-trapping effect is clearly evidenced in the long wavelength range (λ>600 nm). The flat silver mirror results in double-pass absorption with an increase of the short-circuit current of ΔJsc=4.4 mA/cm^2. With the nanostructured back mirror, numerous overlapping resonances contribute to further absorption enhancement and result in an additional ΔJsc=4.5 mA/cm^2. Theoretical short-circuit current densities J_{th} sum up to J_{th}=25.6 mA/cm² for structure C. The measured EQE exhibits less pronounced resonances due to fabrication imperfections, but similar average absorption. The cross-section maps of the generation rates displayed in Figure 3(c) for 1 µm-thick GaAs solar cells and structures A, B and C illustrate the spectacular increase of the density of photogenerated carriers, as a result of efficient light trapping in a 205 nm-thick GaAs layer.

To gain more insights in the mechanism of optical resonances, labeled α, β and γ in Figure 3(b), we calculate 1-R, where R is the specular reflectance at normal incidence as a function of the wavelength and

grating period p. Figure 3(e) shows the result obtained for nanostructured TiO_2/Ag back mirror with a fixed grating height h=120 nm and a square width-to-period ratio (d/p=0.6). This dispersion diagram features numerous resonances with two different behaviors. In the 400–600 nm wavelength range, absorption peaks are insensitive to the grating period. These resonances are attributed to vertical Fabry-Perot (FP) modes. The same features can be observed with a flat mirror, and the resonance wavelengths depend mainly on the total thickness of the layer stack. The resonant conditions are given by

$$2\sum_i k_{z,i} h_i + \varphi = 2\pi q \quad (1)$$

where $k_{z,i}=2\pi n_i/\lambda$ is the z-component wavevector at normal incidence in layer i (thickness h_i and refractive index n_i), λ is the wavelength and the integer q defines the FP order. The phase change φ induced by reflection at the top and bottom interfaces is evaluated from the complex Fresnel coefficients. The result is shown in Figure 3(e) (green dashed lines) for the two FP resonances α_1 and α_2 found at short wavelengths. They correspond to FP orders q=6 and q=7 (labeled FP_6 and FP_7, respectively). The low contrast of these resonance peaks is due to the high absorption and efficient DLARC in this wavelength range.

In the long wavelength range (λ>600 nm), the absorption peaks exhibit a strong period dependence and are attributed to guided-mode resonances. The grating scatters light into diffracted waves of orders (m_1,m_2) defined by their in-plane wavevectors:

$$\vec{k}_{//\,(m_1,m_2)} = \vec{k}_{//\,(00)} + m_1 \frac{2\pi}{p}\vec{e}_x + m_2 \frac{2\pi}{p}\vec{e}_y \quad (2)$$

where $\vec{k}_{//\,(00)}$ is the in-plane wavevector of incident waves and (m_1,m_2) are integers. The additional in-plane momentum induced by the grating allows coupling through ether transverse-electric (TE) or transverse-magnetic (TM) guided waves propagating in the solar cells. The approximate resonance wavelengths are calculated using a model of planar waveguide (35), taking into account the quasi-periodic boundary condition for the in-plane component (Equation (2)). The coupling between guided modes is not taken into account in this simple model. Nevertheless, it allows to fit and to identify the main resonances: β_1 and β_3 are TE guided modes coupled to the diffracted orders (±1, ±1), β_2 and β_5 are TM guided modes coupled to the diffracted orders (±1, 0), β_4 is TE guided mode coupled to the diffracted orders (±1, 0), γ_1 and γ_2 are TE and TM guided modes coupled to the diffracted orders (±2,0), respectively. The corresponding dispersion curves are plotted in Figure 3(e) and agree with rigorous numerical calculations. They exhibit different slopes related to the different diffracted orders. The origin and characteristics of both Fabry-Perot and guided-mode resonances are further confirmed by their angular dependence, and by the number and position of nodes and anti-nodes in the field distributions (see Supplementary Note 1 and 3 and Supplementary Figures 5 and 7). Overall, the integrated absorption maintains a high short-circuit current

(J_{th}>25 mA/cm² up to 45°, J_{th}>23.5 mA/cm² up to 60°) through overlaps of multiple resonances (Figure 3(f)).

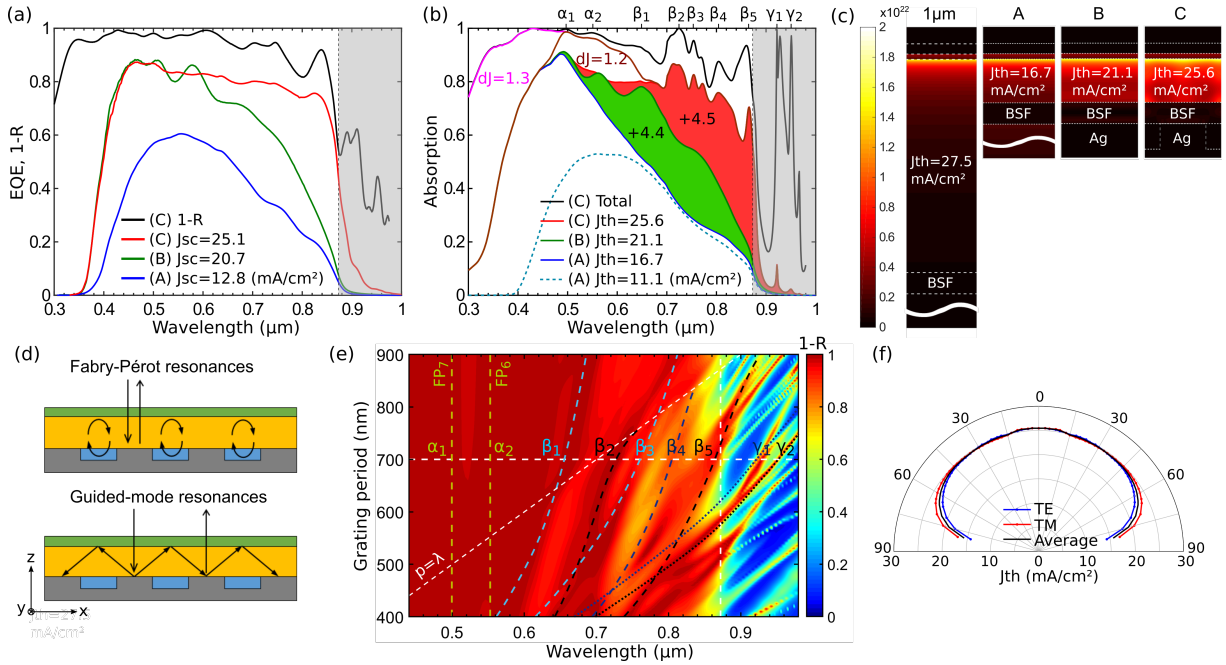

Figure 3: Optical analysis of the ultrathin GaAs solar cells. (a) EQE measurement for 3 different types of solar cells: (A) as-grown on a GaAs substrate, (B) with a flat Ag back mirror and (C) with a nanostructured Ag back mirror. 1-R (solar cells C) is also plotted (black curve). (b) Calculation of optical absorption in 205 nm-thick GaAs for the same structures. Structure A: as-grown with a single-layer ARC (dashed) or with the same design as B (reverse order without back mirror). Structure C: detailed absorption in each III-V layer (AlInP sum up to dJ=1.3mA/cm^2, AlGaAs: dJ=1.2mA/cm^2). (c) Cross-section maps of the generation rate in 1µm-thick GaAs solar cells (DLARC, as-grown), and structures A, B and C (see Supplementary Note 2). (d) A schematic of the different types of resonances. (e) Dispersion diagram of 1-R as a function of the illumination wavelength and the period of the diffraction grating. Dashed curves are resonance wavelengths calculated with analytical models (see text for details). (f) Polar plot of the calculated J_{sc} as a function of the incident angle in 205 nm-thick GaAs (structure C).

5. Loss analysis and path toward 25% efficiency

In this section, we analyze the performance of the ultrathin solar cell with a nanostructured mirror and discuss the possibility to achieve even higher efficiency. Figure 4(a) summarizes the detailed loss analysis for J_{sc}, FF and V_{oc}: our experimental results are shown in bold and top values correspond to radiative limits. The J_{sc} reference of 31.9 mA/cm² is calculated for 205 nm-thick GaAs using an approximate lambertian light-trapping model (5,6). We measured J_{sc}=24.6 mA/cm² and the highest EQE without front contact shading (5–6% of the total area) results in J_{sc}=25.1 mA/cm², close to the numerical calculation of 25.6 mA/cm² for the optimized TiO_2/Ag back mirror. Small discrepancy is due to the actual shape of fabricated structures. Parasitic optical losses contain absorption in the window layer (dJ=1.3 mA/cm²), in the BSF (dJ=1.2 mA/cm²), in the Ag mirror (dJ=2.7 mA/cm²) and due to

reflection (dJ=1.1 mA/cm²). Parasitic absorption in the metallic reflector can be avoided through a combination of high-index-contrast gratings with all-dielectric or hybrid dielectric/metallic mirrors (36,37). The stack of semiconductor heterostructures needs further optimization to reduce the thickness of the AlInP and AlGaAs layers and improve collection of photogenerated carriers in these layers. The shape of the nanostructured back mirror could be also optimized to improve light-trapping. For instance, replacing squares by L-shape or blazed nanostructures breaks a plane of symmetry and should increase the number of resonance modes by a factor of two. Overall, assuming half of the optical losses are recovered leads to a short-circuit current over 28 mA/cm².

To analyze the electronic characteristics of the solar cells, 1-sun JV curves are fitted using a two-diode model with a fixed Jsc and diode idealities of 1 and 2 (38). An example of fit is given in Figure 4(b), showing the absolute values of $J(V) - J_{sc}$ in logarithmic scale and different components of the two-diode model. The fitted parameters are: $J_{01}=2.8\times10^{-17}$ mA/cm², $J_{02}=4.3\times10^{-8}$ mA/cm², $R_p=2.4\times10^{3}$ ohm cm² and $R_s=0.8$ ohm cm². This procedure is repeated for every solar cell of different surface areas of 1×1, 2×2 and 3×3 mm². The V_{oc} decreases with the cell size and is correlated with an increased dark current density J_{02}. The size-dependence of the recombination current is observed in GaAs (39) and can be recovered through edge passivation using S-based chemicals (40). In Figure 4(c), we plot the J_{02} values as a function of the perimeter-to-surface ratio (P/A). The linear trend allows to decompose J_{02} into a surface area component $J_{02,A}$ and a perimeter component $J_{02,P}$ (41):

$$J_{02} = J_{02,A} + J_{02,P}\frac{P}{A} \quad (3)$$

For large-area solar cells, edge recombination is suppressed. J_{02} reaches $J_{02,A}=8.7\times10^{-9}$ mA/cm².and results in an increase of V_{oc} up to 1.045 V and FF up to 0.826. The corresponding JV characteristics are plotted in Figure 4(d). Further improvements of the fill factor are expected with improved parallel and series resistances: FF=0.84 for $R_p=10^6$ ohm cm² and FF=0.857 for $R_s=0$. The visible shunt conductance under illumination may be due to native oxides across the p-n junction at the edge or degradation from process steps after the mesa edges are revealed by chemical etching. The series resistance can be further optimized with GeAu alloys (42) and a smaller spacing of contact grids. To achieve even higher FF, the dark current density J_{02} should be lowered down to about 10^{-9} mA/cm² (3).

Regarding V_{oc}, we calculate the radiative limit using the detailed balance principle applied for 205 nm-thick GaAs solar cells (26, 43, 44) (see Supplementary Note 5). The calculated limit efficiency (25°C, illumination AM1.5G spectrum) is $\eta = 24.6\%$ for the cell with a flat mirror (J_{sc}=23.4 mA/cm², V_{oc}=1.172 V, FF=0.896) and $\eta = 32.3\%$ for the cell with lambertian light-trapping

(J_{sc}=31.9 mA/cm², V_{oc}=1.132 V, FF=0.893). We note that the Voc radiative limit is reduced by 40 meV for lambertian light-trapping as compared to a flat mirror because of enhanced radiative emission (photonic bandgap narrowing, BGN). However, most of the Voc loss in our devices originates from non-radiative recombination (see Figure 4(d)). The choice of high doping is favorable for lateral conductivity and a high built-in potential in ultrathin absorber, but p-type GaAs is known for the bandgap narrowing (BGN) effect which lowers the bandgap by about 26 meV at the doping concentration of 10^{18} cm^{-3} (45). To achieve high V_{oc}, reducing non-radiative loss and maintaining efficient photon recycling are of upmost important. Based on the above discussion, an efficiency of 25% (J_{sc}=28 mA/cm², V_{oc}=1.05 V, FF=0.85) appears as a realistic target for 205 nm-thick GaAs solar cells with an optimized design.

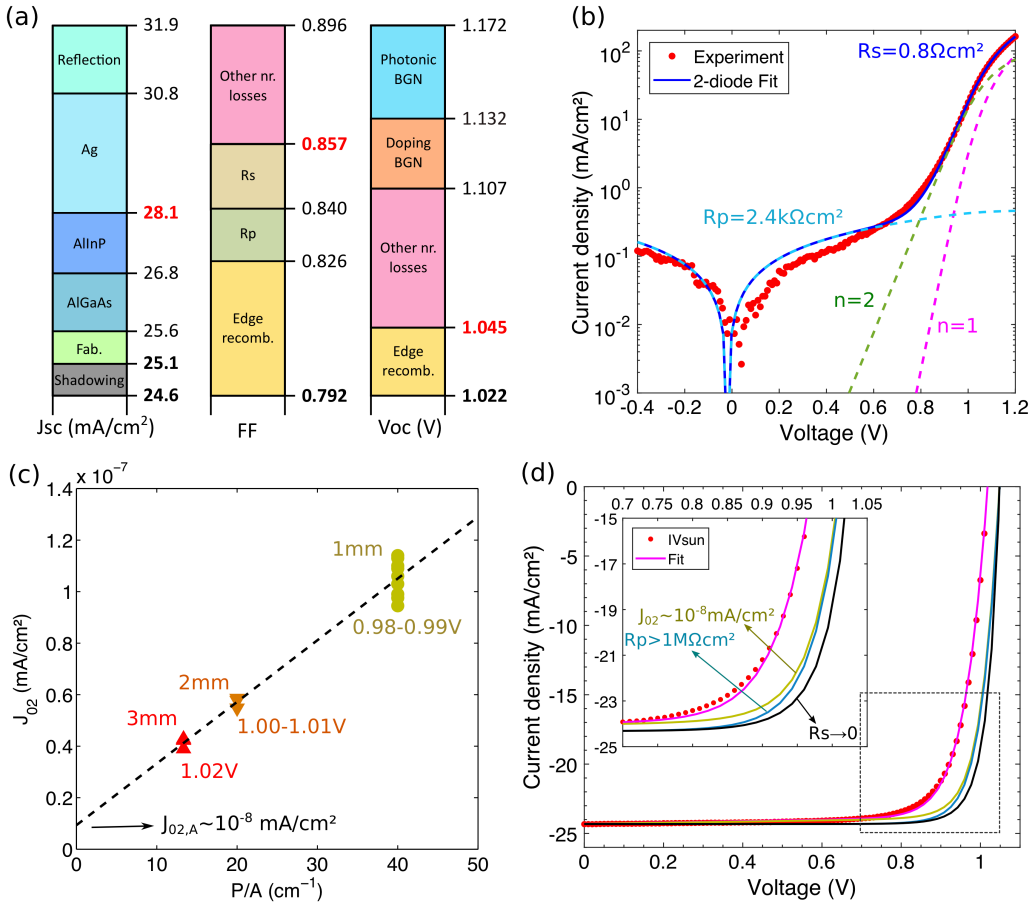

Figure 4: Current-voltage characteristics and loss analysis. (a) Detailed loss analysis for J_{sc}, FF and V_{oc}. The different colors represent the different origins of losses that fill the gap between measurements (bold) and the radiative limit for 205 nm GaAs absorber (top values). Intermediate values in red appear as a realistic short-term target that corresponds to a conversion efficiency of 25%. (b) Typical JV curve under 1 sun illumination shifted with J_{sc} in log scale (red dot: J-J_{sc}) and fit with a two-diode model (blue curve). Different components of the model are shown in dashed lines. (c) Correlation of the J_{02} saturation current density with the perimeter-to-surface ratio P/A. Dashed line: linear fit of J_{02} values extracted from square solar cells of width 3mm (3 devices), 2mm (3 devices) and 1mm (9 devices) (see also Supplementary Figs 2 and 3). (d) JV characteristics of the record solar cell and the fit. Efficiency can be increased by successive improvements of fitted parameters (see the main text): saturation current density J_{02} (yellow green curve), shunt resistance (blue curve) and series resistance (black curve). Inset shows a zoom around the maximum power point.

6. Conclusion

In conclusion, we have conceived and fabricated ultrathin GaAs solar cells with a TiO_2/Ag nanostructured back mirror using soft nanoimprint lithography. We achieved a certified efficiency of 19.9% under AM1.5G illumination (J_{sc}=24.64 mA/cm², V_{oc}=1.022 V, FF=0.792). The EQE exhibits a strong absorption enhancement in the 600–900 nm wavelength range, in agreement with numerical calculations. Broadband absorption is the result of multiple overlapping resonances induced by the nanostructured mirror, identified as Fabry-Perot and guided-mode resonances. We have revealed the origin of optical and electrical losses and proposed routes for further optimizations so that 200 nm-thick ultrathin GaAs solar cell with 25% efficiency appears as a realistic short-term target. These results constitute a very significant improvement over previous experimental achievements and numerical predictions of realistic devices and demonstrate that broadband light trapping is compatible with high performances. These results can find direct applications in flexible, lightweight, and radiation-resistant photovoltaic system for space applications. For large-scale photovoltaics, applying a similar architecture to thin-film solar cells made of CIGS and CdTe opens up promising perspectives for material savings and throughput improvements. In this context, this approach based on nanoimprinting sol-gel could represent a game changer for low cost and large-scale fabrication of nanostructured mirrors compatible with industrial constraints.

Methods

Semiconductor layer stack. The III-V semiconductor layers were grown by Metalorganic Vapor Phase Epitaxy (MOVPE) at the Fraunhofer Institute for Solar Energy Systems (ISE). The layers with target thickness and doping level are given in Supplementary Table 1. Zn and Si were used as p-type and n-type dopants, respectively. The growth was conducted on a n-type GaAs(100) substrate, consisting of buffer GaAs, AlGaAs etch stop (used for the substrate removal), n+GaAs/GaInAs contact layers, n-AlInP window, 205 nm GaAs homojunction as the main absorber, p-AlGaAs back surface field (BSF) and p+GaAs contact layer. Wide-bandgap AlGaAs and AlInP alloys are used to passivate the GaAs surface and act as minority carrier blocking layer to reduce surface recombination losses. The fabrication process of devices was performed at the Centre for Nanoscience and Nanotechnology (C2N) and is sketched in Figure 1.

Localized back contacts fabrication. Localized p-type back contacts consist of 5×5 μm^2 squares regularly spaced with a period of 50 µm in both x- and y-direction on the layer surface defined using photolithography (coverage: 1% of the total surface). After deoxidation of p+GaAs in a dilute HCl solution, localized Ti/Au (20/200 nm) was fabricated using electron-beam assisted evaporation and lift-off. Uncovered area of p+GaAs was etched in a mixture of citric acid at 1 g/L and hydrogen peroxide (30%) with a 5:1 volume ratio. Etching is naturally stopped at top of the AlGaAs layer (BSF).

Nanostructured TiO_2/Ag mirror fabrication. After localized back contacts fabrication a dielectric mirror was fabricated by direct embossing of TiO_2 derived sol-gel film followed by a silver deposition. For the embossing of the TiO_2 sol-gel derived film, we used Degassing Assisted Patterning (DAP) (46), a modified version of Soft Nanoimprint Lithography that allows for a rapid embossing of sol-gel derived films (47). The technique makes use of a degassed polydimethylsiloxane (PDMS) based stamp to improve the resolution and rapidity of the embossing of sol-gel derived films. Unlike other Nanoimprint techniques, replication by DAP is driven by the inner underpressure of the stamp, and therefore does not require the use of an embossing machine. Because no external pressure is applied, DAP induces no long-range pattern deformations, limits short-range deformations, and is thus suitable for large surface area patterning. The PDMS based stamp is first degassed in a dessicator for 10 min. TiO_2 sol-gel hybrid is spin-coated on the AlGaAs surface (BSF) and the PDMS based stamp is then molded (in air). Eventual macroscopic air bubbles surrounding defects and/or localized around the localized back contacts are removed within few seconds through the diffusion of air in the degassed PDMS based stamp. In the same way, the air trapped in the stamp protrusion is aspired inside the stamp and replaced by the TiO_2 sol-gel. The degassed stamp also quickly removes the ethanol and the water expelled during the sol-gel transition (gelation), hydrolysis and condensation occurring when the sol-gel is stabilized at 110°C for 5 min on a hot-plate before the demolding of the stamp. Subsequently, the top surface of the sample (coated with TiO_2 nanostructures) was protected with a photoresist mask, opening only the area of the localized ohmic contacts. The residual of nanoimprinted TiO_2 above the localized contacts was etched by dipping shortly the sample in a dilute HF solution. Ag (200 nm) was then deposited by electron-beam assisted evaporation using a rotating stage with a 10° tilt to the surface normal to ensure conformal deposition of Ag on both localized ohmic contacts and TiO_2 nanostructures. A TiO_2/Ag nanostructured back mirror was thus obtained and acted at the same time as the back electrode.

Bonding and substrate removal. The Ag mirror-side of the sample was bonded to a glass host substrate using ormostamp (flexible hybrid inorganic/organic polymer), which was reticulated under UV light for 20 minutes. The GaAs substrate was etched in a NH_4OH:H_2O_2:H_2O (1:4:15) solution and the AlGaAs etch stop was removed in HF:H_2O (1:20). After this step, the III-V layer stack order was inversed.

Front contacts and anti-reflection coating. The front contacts with grid spacing of 600 or 800 µm were fabricated using the similar steps as localized back contacts. They consist of multilayers of Ni/Au/Ge/Au/Ni/Au (4/10/60/110/10/100 nm) with no post thermal annealing to avoid degradation of the Ag mirror as well as the ultrathin GaAs absorber. Uncovered area of n-GaAs and n-$Ga_{0.87}In_{0.13}As$ were etched in a mixture of citric acid at 1 g/L and hydrogen peroxide (30%) with a 5:1 volume ratio. The final solar cells of 1×1, 2×2 and 3×3 mm² were delimited with photolithography mask and mesa etching in dilute HCl (removing AlInP) and in H_3PO_4:H_2O_2:H_2O (3:1:40) (removing GaAs). MgF_2/Ta_2O_5 (78/48 nm) double-layer anti-reflection coating (DLARC) was deposited using electron-beam assisted evaporation.

Description of the silicon master, PDMS based stamp and sol-gel derived film. *Silicon master fabrication:* the silicon master mold was fabricated by electron beam lithography carried out at 100 keV (Vistec EBPG5000+) using positive-tone PMMA resist (495PMMA A - solids: 7% in Anisole) and anisotropic reactive ion etching based on SF_6/CHF_3 gasses. The Silicon master was treated with 1H,1H,2H,2H-perfluorooctyltriethoxysilane (POTS) by chemical vapor deposition (CVD) method, following a procedure developed in reference (48).

Hard-PDMS/PDMS stamp fabrication: the silicon master is replicated into a composite hard-PDMS/PDMS stamp by using the procedure similar to the one proposed in reference (49). The hard-PDMS/PDMS stamp is finally treated with Trimethylsilyl chloride (TMCS) silanes by chemical vapor deposition method (50).

Sol-gel initial solutions: absolute ethanol was purchased from Normapur, inorganic precursor $TiCl_4$ and F127 Pluronic (EO106-PO70-EO106) were purchased from Aldrich. Dense TiO2 thin films were prepared by spin coating solutions composed of $TiCl_4$:F127:H_2O:EtOH with respective molar ratio of 1:0.0001:10:50. Final solution was obtained by dissolving the precursors $TiCl_4$ in ethanol and water followed by the addiction of a small amount of F127 (to improve the wettability).

Optical simulations and refractive indices. Optical simulations have been performed with the rigorous coupled wave analysis (RCWA) method (31,32,33,34). We choose the x-z plane as the plane of incidence and consider impinging plane waves linearly polarized. We call transverse electric (TE) incident polarization for electric field perpendicular to the incidence plane (along the y-axis), and transverse magnetic (TM) incident polarization for magnetic field perpendicular to the incidence plane. We calculate the absorption in each layer with 20 Fourier order, and the calculation is done for each wavelength. The refractive indices used for optical simulation of ultrathin GaAs solar cells are plotted in Supplementary Figure 4. The refractive indices are taken from reference (51) for Ta_2O_5, from reference (52) for MgF_2 and $Al_{0.42}Ga_{0.58}As$, and from reference (53) for $Al_{0.51}In_{0.49}P$. We use refractive indices of high-purity GaAs (52,54), and we fit the near bandgap extinction coefficients with cubic spline and extend the data in the sub-bandgap region with an exponential Urbach tail of energy width 10 meV for n-GaAs and 20 meV for p-GaAs. Larger band tail is attributed for p-GaAs to simulate the higher sub-bandgap absorption. The refractive index of Ag is taken from the measurement published recently in reference (55) to account for realistic absorption loss in Ag. TiO2 prepared from sol-gel with our process has typical refractive indices about 1.9 at 500 nm and is kept constant over the whole spectrum.

Optimization of the optical design. The geometry of ultrathin GaAs solar cells has been optimized by maximizing the theoretical short-circuit current J_{th}. For the double-layer anti-reflection coating (DLARC) on ultrathin GaAs solar cells with a flat mirror, the best value is obtained for MgF_2/Ta_2O_5 layers of thickness 78/48 nm. For ultrathin GaAs solar cells with a nanostructured Ag back mirror, we use the same DLARC and determine the optimal geometry as: grating height h=120 nm, period p=700 nm, and silver square nanostructures of width 420 nm (60% of the period).

Data availability. The data that support the plots within this paper and other findings of this study are available from the corresponding author upon reasonable request.

1. References

[1] Yoshikawa, K., Kawasaki, H., Yoshida, W., Irie, T., Konishi, K., Nakano, K., Uto, T., Adachi, D., Kanematsu, M., Uzu, H., et al. (2017). Silicon heterojunction solar cell with interdigitated back contacts for a photoconversion efficiency over 26%. Nature Energy *2*, 201732.

[2] Shockley, W., and Queisser, H.J. (1961). Detailed Balance Limit of Efficiency of p-n Junction Solar Cells. Journal of Applied Physics *32*, 510–519.

[3] Kayes, B.M., Nie, H., Twist, R., Spruytte, S.G., Reinhardt, F., Kizilyalli, I., and Higashi, G.S. (2011). 27.6% Conversion efficiency, a new record for single-junction solar cells under 1 sun illumination. In 2011 37th IEEE Photovoltaic Specialists Conference (PVSC), pp. 000004–000008.

[4] Green, M. A.; Hishikawa, Y.; Dunlop, E. D.; Levi, D. H.; Hohl-Ebinger, J.; Yoshita, M. & Ho-Baillie, A. W. Solar cell efficiency tables (Version 53), Progress in Photovoltaics: Research and Applications, 27, 3-12 (2019).

[5] Green, M.A. (2002). Lambertian light trapping in textured solar cells and light-emitting diodes: analytical solutions. Prog. Photovolt: Res. Appl. *10*, 235–241.

[6] Yablonovitch, E. (1982). Statistical ray optics. J. Opt. Soc. Am., JOSA *72*, 899–907.

[7] Hirst, L.C., Yakes, M.K., Warner, J.H., Bennett, M.F., Schmieder, K.J., Walters, R.J., and Jenkins, P.P. (2016). Intrinsic radiation tolerance of ultra-thin GaAs solar cells. Applied Physics Letters *109*, 033908.

[8] Brongersma, M.L., Cui, Y., and Fan, S. (2014). Light management for photovoltaics using high-index nanostructures. Nature Materials *13*, 451–460.

[9] Collin, S. (2014). Nanostructure arrays in free-space: optical properties and applications. Rep. Prog. Phys. *77*, 126402.

[10] Mokkapati, S., and Catchpole, K.R. (2012). Nanophotonic light trapping in solar cells. Journal of Applied Physics *112*, 101101.

[11] Depauw, V., Trompoukis, C., Massiot, I., Chen, W., Dmitriev, A., Roca i Cabarrocas, P., Gordon, I., and Poortmans, J. (2017). Sunlight-thin nanophotonic monocrystalline silicon solar cells. Nano Futures *1*, 021001.

[12] Branham, M.S., Hsu, W.-C., Yerci, S., Loomis, J., Boriskina, S.V., Hoard, B.R., Han, S.E., and Chen, G. (2015). 15.7% Efficient 10-µm-Thick Crystalline Silicon Solar Cells Using Periodic Nanostructures. Advanced Materials *27*, 2182–2188.

[13] Gaucher, A., Cattoni, A., Dupuis, C., Chen, W., Cariou, R., Foldyna, M., Lalouat, L., Drouard, E., Seassal, C., Roca i Cabarrocas, P., et al. (2016). Ultrathin Epitaxial Silicon Solar Cells with Inverted Nanopyramid Arrays for Efficient Light Trapping. Nano Lett. *16*, 5358–5364.

[14] Wang, K.X., Yu, Z., Liu, V., Cui, Y., and Fan, S. (2012). Absorption Enhancement in Ultrathin Crystalline Silicon Solar Cells with Antireflection and Light-Trapping Nanocone Gratings. Nano Letters *12*, 1616-1619.

[15] Kapur, P., Moslehi, M., Deshpande, A., Rana, V., Kramer, J., Seutter, S., Deshazer, H., Coutant, S., Calcaterra, A., Kommera, S., et al. (2013). A Manufacturable, Non-Plated, Non-Ag Metallization Based 20.44% Efficient, 243cm2 Area, Back Contacted Solar Cell on 40um Thick Mono-Crystalline Silicon. 28th European Photovoltaic Solar Energy Conference and Exhibition 2228–2231.

[16] Cariou, R., Benick, J., Feldmann, F., Höhn, O., Hauser, H., Beutel, P., Razek, N., Wimplinger, M., Bläsi, B., Lackner, D., et al. (2018). III–V-on-silicon solar cells reaching 33% photoconversion efficiency in two-terminal configuration. Nature Energy *3*, 326–333.

[17] Goffard, J., Colin, C., Mollica, F., Cattoni, A., Sauvan, C., Lalanne, P., Guillemoles, J.F., Naghavi, N., and Collin, S. (2017). Light Trapping in Ultrathin CIGS Solar Cells with Nanostructured Back Mirrors. IEEE Journal of Photovoltaics *7*, 1433–1441.

[18] van Lare, C., Yin, G., Polman, A., and Schmid, M. (2015). Light Coupling and Trapping in Ultrathin Cu(In,Ga)Se2 Solar Cells Using Dielectric Scattering Patterns. ACS Nano *9*, 9603–9613.

[19] Söderström, K., Haug, F.-J., Escarré, J., Cubero, O., and Ballif, C. (2010). Photocurrent increase in n-i-p thin film silicon solar cells by guided mode excitation via grating coupler. Applied Physics Letters *96*, 213508.

[20] Zhu, J., Hsu, C.-M., Yu, Z., Fan, S., and Cui, Y. (2010). Nanodome Solar Cells with Efficient Light Management and Self-Cleaning. Nano Lett. *10*, 1979–1984.

[21] Liu, W., Wang, X., Li, Y., Geng, Z., Yang, F., and Li, J. (2011). Surface plasmon enhanced GaAs thin film solar cells. Solar Energy Materials and Solar Cells *95*, 693–698.

[22] Nakayama, K., Tanabe, K., and Atwater, H.A. (2008). Plasmonic nanoparticle enhanced light absorption in GaAs solar cells. Applied Physics Letters *93*, 121904.

[23] Massiot, I., Vandamme, N., Bardou, N., Dupuis, C., Lemaître, A., Guillemoles, J.-F., and Collin, S. (2014). Metal Nanogrid for Broadband Multiresonant Light-Harvesting in Ultrathin GaAs Layers. ACS Photonics *1*, 878–884.

[24] Atwater, H.A., and Polman, A. (2010). Plasmonics for improved photovoltaic devices. Nat Mater *9*, 205– 213.

[25] Vandamme, N., Chen, H., Gaucher, A., Behaghel, B., Lemaitre, A., Cattoni, A., Dupuis, C., Bardou, N., Guillemoles, J., and Collin, S. (2015). Ultrathin GaAs Solar Cells With a Silver Back Mirror. IEEE Journal of Photovoltaics *5*, 565–570.

[26] Miller, O.D., Yablonovitch, E., and Kurtz, S.R. (2012). Strong Internal and External Luminescence as Solar Cells Approach the Shockley-Queisser Limit. IEEE Journal of Photovoltaics *2*, 303–311.

[27] Steiner, M.A., Geisz, J.F., García, I., Friedman, D.J., Duda, A., and Kurtz, S.R. (2013). Optical enhancement of the open-circuit voltage in high quality GaAs solar cells. Journal of Applied Physics *113*, 123109.

[28] Walker, A.W., Höhn, O., Micha, D.N., Bläsi, B., Bett, A.W., and Dimroth, F. (2015). Impact of Photon Recycling on GaAs Solar Cell Designs. IEEE Journal of Photovoltaics *5*, 1636–1645.

[29] Yang, W., Becker, J., Liu, S., Kuo, Y.-S., Li, J.-J., Landini, B., Campman, K., and Zhang, Y.-H. (2014). Ultra-thin GaAs single-junction solar cells integrated with a reflective back scattering layer. Journal of Applied Physics *115*, 203105.

[30] Lee, S.-M., Kwong, A., Jung, D., Faucher, J., Biswas, R., Shen, L., Kang, D., Lee, M.L., and Yoon, J. (2015). High Performance Ultrathin GaAs Solar Cells Enabled with Heterogeneously Integrated Dielectric Periodic Nanostructures. ACS Nano *9*, 10356–10365.

[31] Lalanne, P., and Hugonin, J.P. Reticolo software for grating analysis. https://www.lp2n.institutoptique.fr/Membres-Services/Responsables-d-equipe/LALANNE-Philippe

[32] Lalanne, P., and Jurek, M.P. (1998). Computation of the near-field pattern with the coupled-wave method for transverse magnetic polarization. Journal of Modern Optics *45*, 1357–1374.

[33] Lalanne, P., and Morris, G.M. (1996). Highly improved convergence of the coupled-wave method for TM polarization. J. Opt. Soc. Am. A *13*, 779–784.

[34] Li, L. (1997). New formulation of the Fourier modal method for crossed surface-relief gratings. J. Opt. Soc. Am. A, *14*, 2758–2767.

[35] Yeh, P. (1988). Optical waves in layered media (New York : Wiley).

[36] Barugkin, C., Beck, F.J., and Catchpole, K.R. (2017). Diffuse reflectors for improving light management in solar cells: a review and outlook. J. Opt. *19*, 014001

[37] Fu, S.M., Lai, Y.-C., Tseng, C.W., Yan, S.L., Zhong, Y.K., Shen, C.-H., Shieh, J.-M., Li, Y.-R., Cheng, H.-C., Chi, G., et al. (2015). Approaching conversion limit with all-dielectric solar cell reflectors. Opt. Express, *23*, A106–A117.

[38] Suckow, S. 2-3 diode fit. (2014). https://nanohub.org/resources/14300

[39] Ochoa, M., Algora, C., Espinet-González, P., and García, I. (2014). 3-D modeling of perimeter recombination in GaAs diodes and its influence on concentrator solar cells. Solar Energy Materials and Solar Cells *120*, 48–58.

[40] Sheldon, M.T., Eisler, C.N., and Atwater, H.A. (2012). GaAs Passivation with Trioctylphosphine Sulfide for Enhanced Solar Cell Efficiency and Durability. Adv. Energy Mater. *2*, 339–344.

[41] Espinet-González, P., Rey-Stolle, I., Ochoa, M., Algora, C., García, I., and Barrigón, E. (2015). Analysis of perimeter recombination in the subcells of GaInP/GaAs/Ge triple-junction solar cells. Prog. Photovolt: Res. Appl. *23*, 874–882.

[42] Shen, T. C., Gao, G. B., and Morko, H. (1992). Recent developments in ohmic contacts for III-V compound semiconductors. J. Vac. Sci. Techno. B 10, 2113.

[43] Sandhu, S., Yu, Z., and Fan, S. (2013). Detailed balance analysis of nanophotonic solar cells. Opt. Express, *21*, 1209–1217.
[44] Xu, Y., Gong, T., and Munday, J.N. (2015). The generalized Shockley-Queisser limit for nanostructured solar cells. Scientific Reports *5*, 13536.
[45] Jain, S.C., McGregor, J.M., and Roulston, D.J. (1990). Band-gap narrowing in novel III-V semiconductors. Journal of Applied Physics *68*, 3747–3749.
[46] Luo, C., Ni, X., Liu, L., Nomura, S. M., Chen, Y. (2010). Degassing-assisted patterning of cell culture surfaces. Biotechnology and Bioengineering, 105, 854-859.
[47] Dalstein, O., Ceratti, D.R., Boissière, C., Grosso, D., Cattoni, A., and Faustini, M. (2016). Nanoimprinted, Submicrometric, MOF-Based 2D Photonic Structures: Toward Easy Selective Vapors Sensing by a Smartphone Camera. Advanced Functional Materials *26*, 81–90.
[48] Wang, L., Wei, J., and Su, Z. (2011). Fabrication of Surfaces with Extremely High Contact Angle Hysteresis from Polyelectrolyte Multilayer. Langmuir *27*, 15299–15304.
[49] Odom, T.W., Love, J.C., Wolfe, D.B., Paul, K.E., and Whitesides, G.M. (2002). Improved pattern transfer in soft lithography using composite stamps. Langmuir : The ACS Journal of Surfaces and Colloids, Langmuir : The ACS Journal of Surfaces and Colloids., Langmuir®: The ACS Journal of Surfaces and Colloids *18*, 5314–5320.
[50] Cattoni, A., Cambril, E., Decanini, D., Faini, G., and Haghiri-Gosnet, A.M. (2010). Soft UV-NIL at 20 nm scale using flexible bi-layer stamp casted on HSQ master mold. Microelectronic Engineering *87*, 1015– 1018.
[51] Gao, L., Lemarchand, F., and Lequime, M. (2012). Exploitation of multiple incidences spectrometric measurements for thin film reverse engineering. Opt. Express, *20*, 15734–15751.
[52] Palik, E.D. (1997). Handbook of Optical Constants of Solids (San Diego: Academic Press).
[53] Schubert, M., Woollam, J.A., Leibiger, G., Rheinländer, B., Pietzonka, I., Saß, T., and Gottschalch, V. (1999). Isotropic dielectric functions of highly disordered AlxGa1−xInP lattice matched to GaAs. Journal of Applied Physics *86*.
[54] Sturge, M.D. (1962). Optical Absorption of Gallium Arsenide between 0.6 and 2.75 eV. Phys. Rev. *127*, 768–773.
[55] Jiang, Y., Pillai, S., and Green, M.A. (2016). Realistic Silver Optical Constants for Plasmonics. Scientific Reports *6*, 30605.

Acknowledgements

The authors acknowledge fruitful discussions with Jean-François Guillemoles, electromagnetic simulation support from Philippe Lalanne, Jean-Paul Hugonin and Christophe Sauvan, and financial support through the French ANR project NANOCELL (grant no. ANR-15-CE05-0026) and the French Renatech network.

Author contributions

HLC carried out most of the fabrication steps for the solar cell experiments at C2N and performed optical modeling and results analysis. AW, OH, DL and FD designed the optimized GaAs solar cell layer structure, DL was writing the recipe for the epitaxy growth and GS evaluated characterization results in the Fraunhofer ISE CalLab. HLC, AC, RDL, MF, NV, JG, BB, CD, and NB developed and optimized the fabrication process. AC and MF specifically developed the nanoimprint process of TiO_2 sol-gel films. NV contributed to the design and modeling of the devices. AC and SC developed the concept of ultrathin solar cells with a nanostructured back mirror and supervised the project. HLC and SC wrote the manuscript. All co-authors participated in the discussions and improvements of the manuscript.

Competing interests

The authors declare no competing interests.

Additional information

Supplementary information is available for this paper.

Correspondence and requests for materials should be addressed to S.C.

Supplementary Information

19.9%-efficient ultrathin solar cell based on a 205nm-thick GaAs absorber and a silver nanostructured back mirror

Hung-Ling Chen[1], Andrea Cattoni[1], Romaric De Lépinau[1,2], Alexandre W. Walker[3,5], Oliver Hoehn[3], David Lackner[3], Gerald Siefer[3], Marco Faustini[4], Nicolas Vandamme[1], Julie Goffard[1,2], Benoît Behaghel[1], Christophe Dupuis[1], Nathalie Bardou[1], Frank Dimroth[3], Stéphane Collin[1,2*]

[1] *Centre for Nanoscience and Nanotechnology (C2N), CNRS, University Paris-Sud / Paris-Saclay, 91120 Palaiseau, France*

[2] *Institut Photovoltaïque d'Ile-de-France (IPVF) – 91120 Palaiseau, France*

[3] *Fraunhofer Institute for Solar Energy Systems (ISE), 79110 Freiburg, Germany*

[4] *Sorbonne Université, UPMC Univ Paris 06, CNRS, Collège de France, Chimie de la Matière Condensée de Paris, 75005 Paris, France*

[5] *Present address: National Research Council of Canada, Ottawa, Ontario K1A 0R6, Canada*

**email: stephane.collin@c2n.upsaclay.fr*

Supplementary Table 1: Description of the III-V semiconductor layers grown by MOVPE. The growth sequence begins from the bottom to the top of the table. Target thickness and doping level of each layer are indicated.

Material	Function	Thickness (nm)	Doping (cm^{-3})
p-GaAs	Contact layer	300	9.0E+18
p-$Al_{0.4}Ga_{0.6}As$	BSF	100	2.0E+18
p-GaAs	Base	100	1.0E+18
i-GaAs		5	i
n-GaAs	Emitter	100	-1.0E+18
n-AlInP	Window	25	-2.0E+18
n-$Ga_{0.87}In_{0.13}As$	Cap (Si) layer	100	-5.0E+18
n-GaAs	Cap (Si) layer	250	-9.0E+18
n-AlGaAs	Etch stop	300	-1.0E+18
n-GaAs	Buffer	250	-5.0E+18

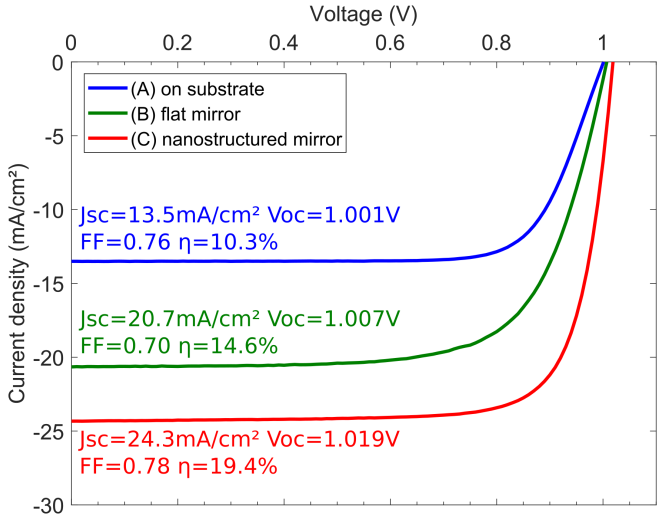

Supplementary Figure 1: Comparison of current-voltage characteristics of ultrathin solar cells under 1 sun illumination. (A) as-grown on a GaAs substrate, (B) with a flat Ag back mirror and (C) with a nanostructured Ag back mirror.

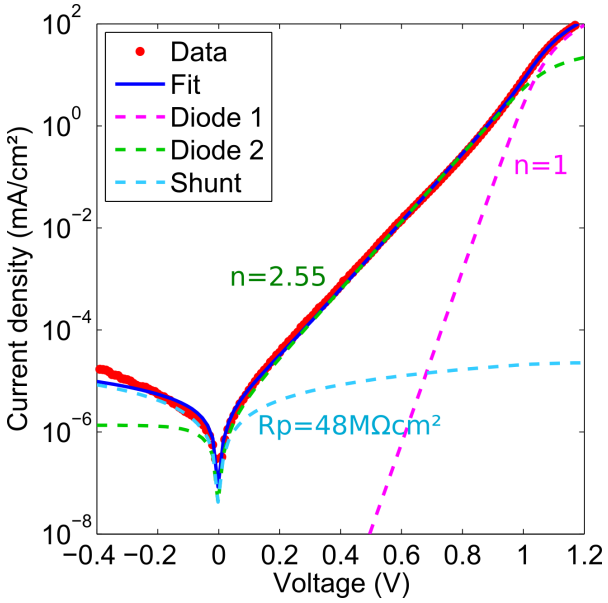

Supplementary Figure 2: Typical dark J-V characteristics for an ultrathin GaAs solar cell with a nanostructured mirror (red dots) and the fit (blue curve). Different components of the two-diode model are shown with dashed lines.

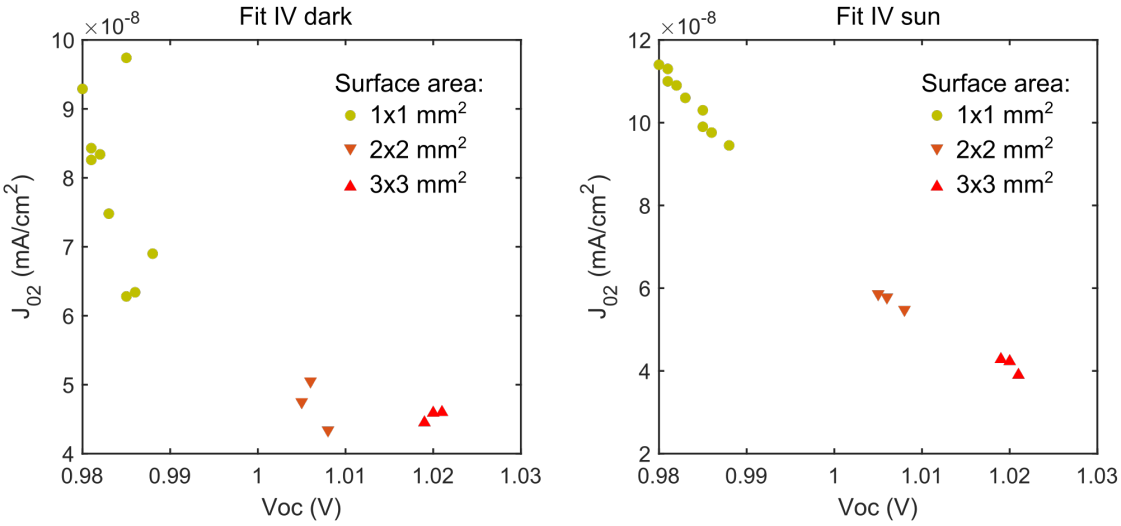

Supplementary Figure 3: Correlation between the saturation current density J_{02} and V_{oc} for the GaAs solar cells of different sizes. Solar cells from the same sample with a nanostructured mirror. (Left) J_{02} obtained by fitting dark IV curves. (Right) J_{02} obtained by fitting 1-sun IV curves.

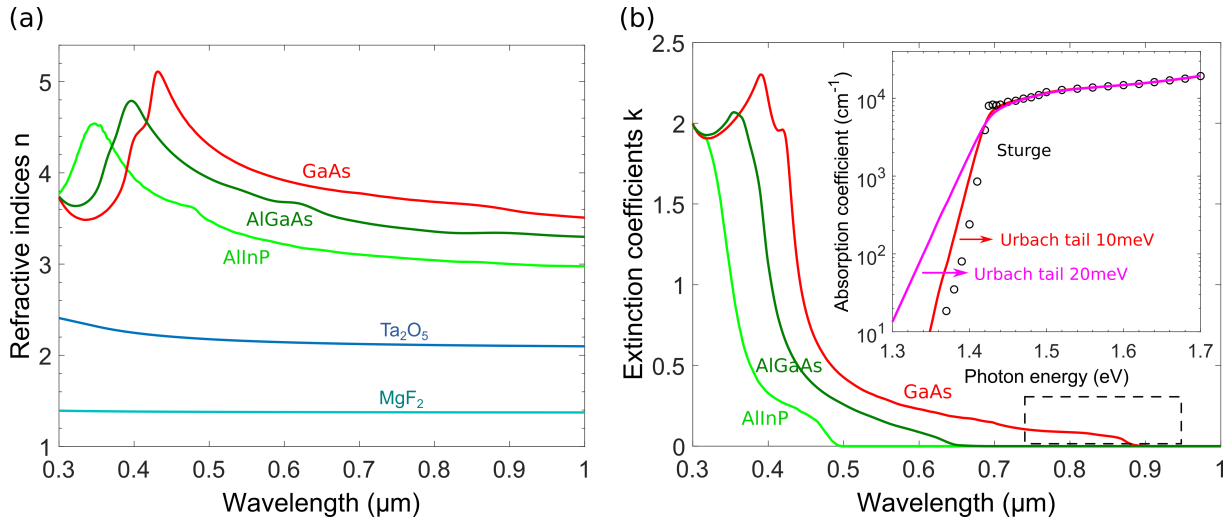

Supplementary Figure 4: Refractive indices of the materials used for optical simulation of ultrathin GaAs solar cells. (a) Real part. (b) Imaginary part. The inset shows the absorption coefficient of high-purity GaAs from Sturge and extension with an Urbach tail below bandgap.

Supplementary Note 1: Analysis of resonant modes

The absorption spectra are shown in Figure 3(b). Several resonant wavelengths are labeled: α_1, α_2, β_1, β_2, β_3, β_4, β_5, γ_1, γ_2. The corresponding cross-section maps of electromagnetic field intensities are displayed in Supplementary Figure 5. Resonances α_1 and α_2 resemble vertical Fabry-Perot modes with horizontally constant field intensities. At longer wavelengths, lateral variations of field intensities suggest the coupling of incident light to guided-mode resonances propagating in the high-index layers. The distributions of the electromagnetic field intensity obtained from exact RCWA calculations are compared with the electromagnetic field amplitudes deduced from a semi-analytical planar waveguide model [1]. We consider a planar layer of total thickness *t* with a refractive index n_2 approximated as the thickness-weighted average of all III-V semiconductor and dielectric refractive indices used in the solar cells (MgF_2, Ta_2O_5, AlInP, GaAs, AlGaAs, and TiO_2). The incident medium is air with refractive index n_1=1, and the substrate is silver with refractive index n_3. TE and TM modes of Maxwell equations are solved in the configuration of a planar waveguide by considering the continuity of tangential components of electromagnetic fields across the interfaces. The resulting field distributions are shown in Supplementary Figure 5 and compared with exact RCWA calculations. These resonances are identified as $TE_q(m_1,m_2)$ and $TM_q(m_1,m_2)$, where the integer q characterizes the order of vertical oscillations (q=0 corresponds to the fundamental mode) and (m_1,m_2) characterizes the orders of diffraction. For example, $TE_{3(1,0)}$ presents 4 field amplitude maximums in the layer thickness and (1,0) represent the 1^{st} order guided mode propagating in the x-direction. On the other hand, (1,1) orders characterize the guided wave propagating in the diagonal of x- and y-axis. For higher diffraction orders, we observe strong field enhancements in the III-V layers, hence n_2 is the refractive index of GaAs and the total thickness *t* is fitted around the total thickness of III-V layers to match the resonant wavelengths from exact RCWA calculations.

For a given guided mode, we calculate the resonance wavelengths for each grating period. The resulting dispersion relations are plotted in Figure 3(e) and reproduce accurately the peaks calculated by RCWA calculations.

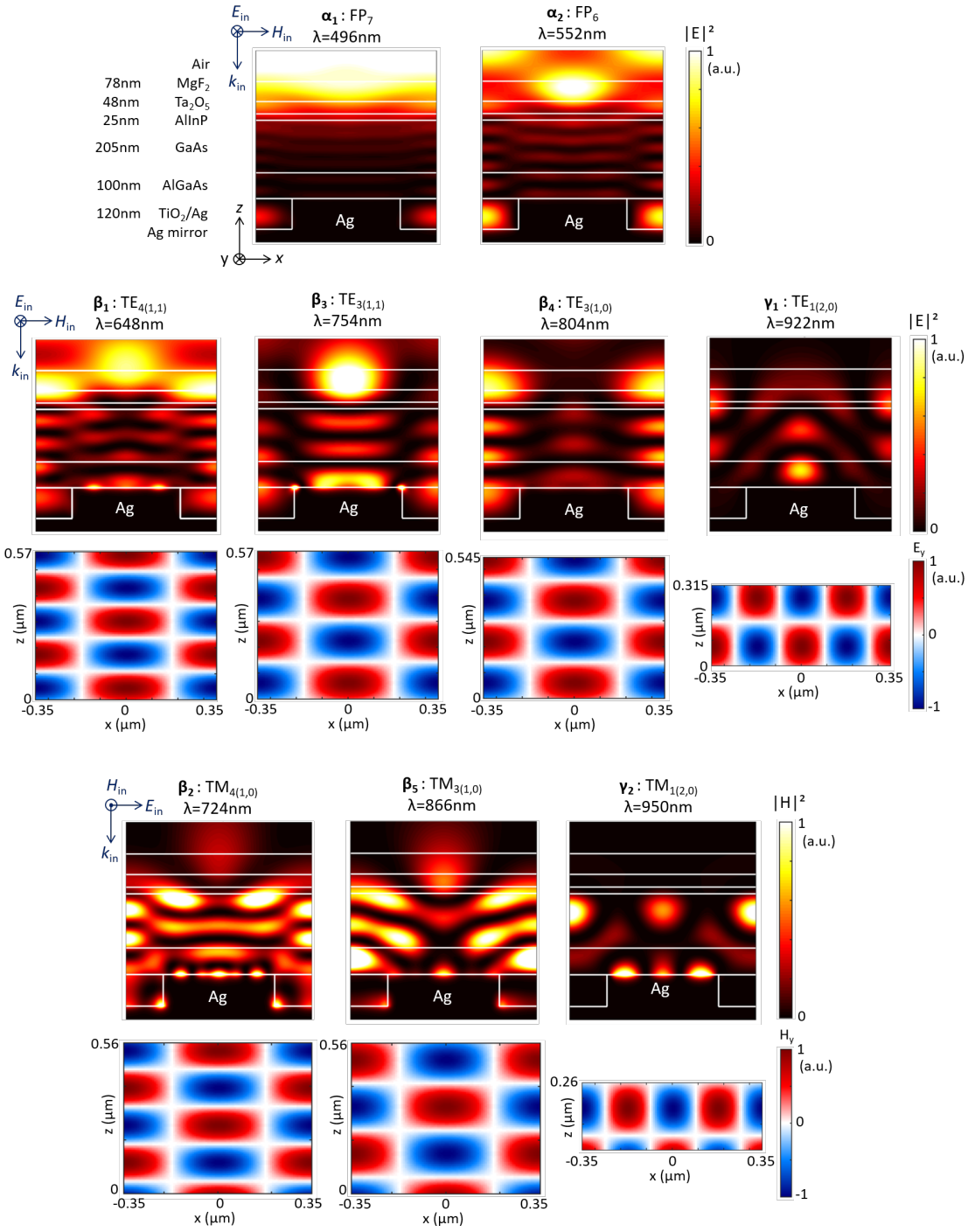

Supplementary Figure 5: Cross-sections of the electric-field intensity $|E|^2$ or magnetic-field intensity $|H|^2$ calculated by RCWA in the optimized 205 nm-thick GaAs solar cell at each resonance wavelength. They are compared to the electric- or magnetic-field amplitude calculated with the semi-analytical approach for guided-modes (blue-red color scale). α_1 and α_2 are attributed to FP resonances labeled by FP_q. For longer wavelengths, $TE_q(m_1,m_2)$ or $TM_q(m_1,m_2)$ guided-mode resonances are identified by the electromagnetic field patterns.

Supplementary Note 2: Photogeneration rate density

To visualize the spatial distribution of the photogeneration rate density, we calculate the average electromagnetic power absorbed in an elementary volume of a material, which is given by the divergence of the Poynting vector: $\nabla \cdot \boldsymbol{S} = \frac{1}{2}\omega\epsilon''|\boldsymbol{E}|^2$ where ω is the frequency of a monochromatic impinging wave, ϵ'' is the imaginary part of the permittivity and $|E|$ is the magnitude of the electric field. Therefore, the carrier generation rate in semiconductor layers (per unit time and volume) can be related to the photon absorption rate integrated over the AM1.5G solar spectrum, assuming that absorption of one photon creates one electron-hole pair. Map of the photogeneration rate density is plotted in Supplementary Figure 6(a). The values are averaged along the y-direction for the TE incident polarization. The density of photogenerated carriers in the absorber is inhomogeneous due to the two-dimensional pattern of the back mirror. Supplementary Figure 6(b) shows the generation rate averaged in both x- and y-direction (polarization-independent because of the symmetry of the structure). We can observe that the z-profile of the carrier generation rate is not homogenous even in a 205 nm thin GaAs absorber with a back reflector, due to the strong absorption coefficient difference between high- and low-energy photon.

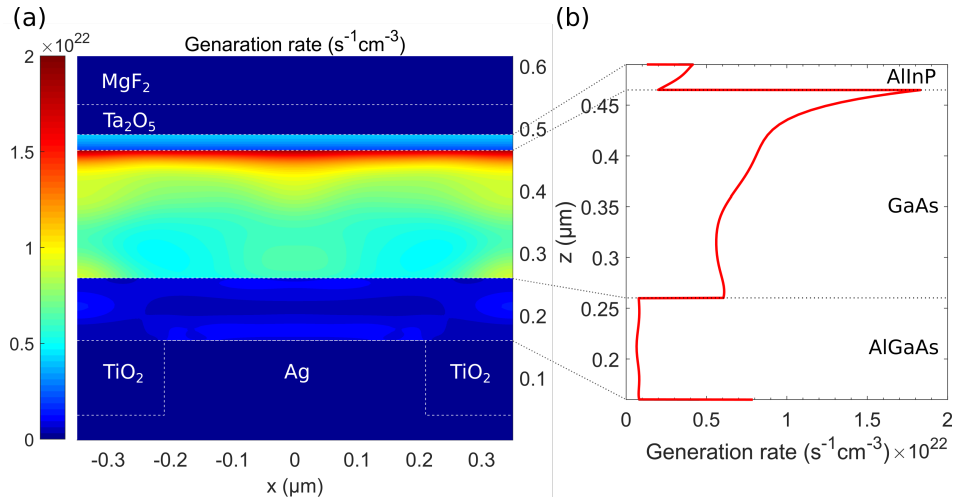

Supplementary Figure 6: Generation rate profiles in an ultrathin GaAs solar cell with a nanostructured back mirror under normal incidence AM1.5G illumination. (a) x-z cross-section of the generation rate averaged over y-direction for the TE incident polarization. (b) z-profile of the generation rate averaged over x and y.

Supplementary Note 3: Angular dependence of optical absorption

Supplementary Figure 7 presents the maps of total absorption spectra (a,b) and absorption in GaAs (c,d) as functions of the incidence angle, for both TE (a,c) and TM (b,d) polarizations. In the short wavelength range (0.3–0.7 μm), the absorption enhancement results from vertical Fabry-Pérot resonances and little variation with the incidence angle is observed due to thin GaAs layer and its high refractive index. In the long wavelength range (0.7–1 μm), strong angular dispersion is related to waveguide-coupled (also named guided-mode) resonances.

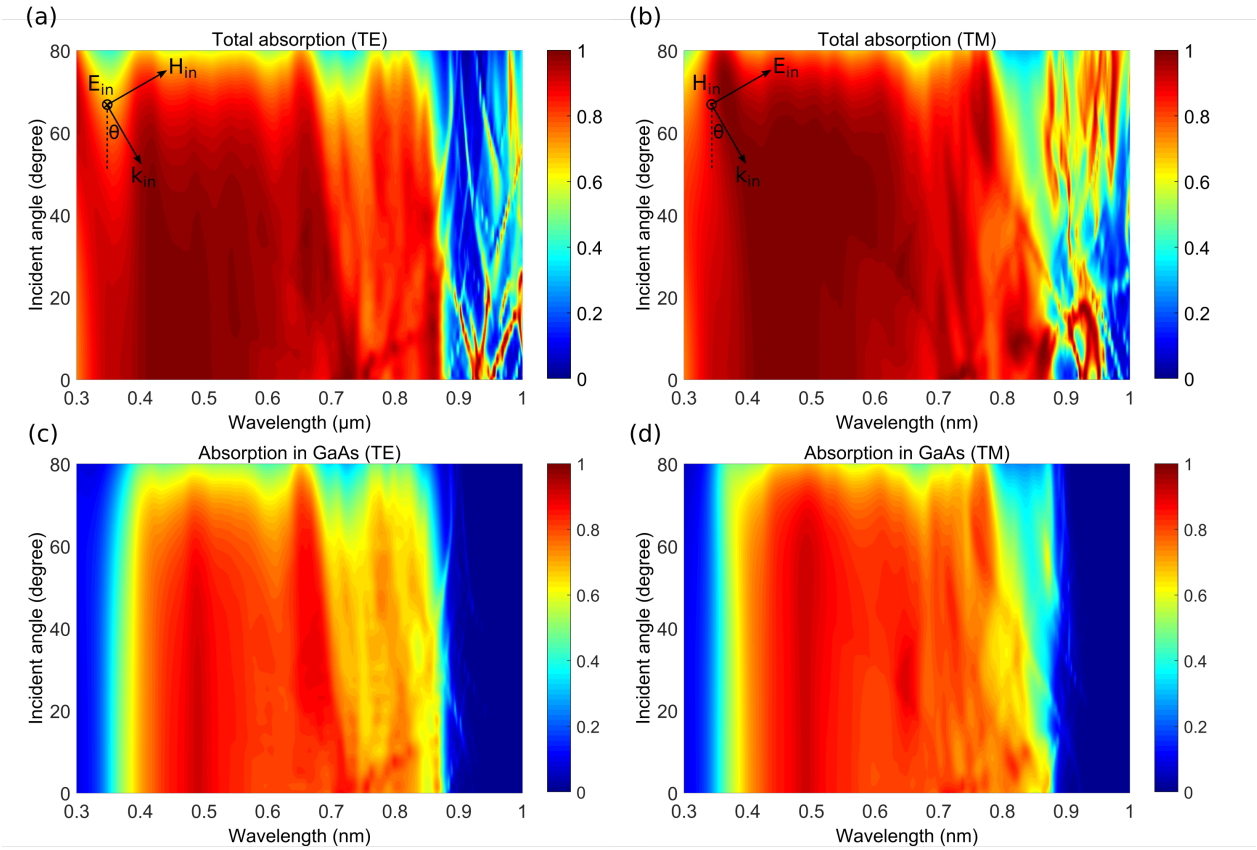

Supplementary Figure 7: Two-dimensional plots of the absorption as a function of the incident angle. The angular dependence of the absorption is calculated for (a,c) TE incident polarization and for (b,d) TM incident polarization. (a,b) show the total absorption and (c,d) show the absorption in GaAs.

Supplementary Note 4: Comparison between measured EQE and simulated absorption

In Supplementary Figure 8, the EQE is compared to the absorption in the GaAs layer, in the (GaAs+AlGaAs) layers, and in the (GaAs+AlGaAs+AlInP) stack. Regarding the absorption in the AlGaAs layer, its maximal contribution to the overall short-circuit current is calculated to be 1.2mA/cm2. However, the low mobility of minority carriers in this layer (high doping and indirect bandgap) and the high surface recombination velocity at the back interface hinder the collection of photogenerated carriers. The effective contribution of the AlGaAs is estimated to less than 3% of the total (0.6mA/cm2). Indeed, the EQE exhibits a trend similar to the absorption calculated in the GaAs layer in the whole 400-800nm wavelength range, with no visible increase of EQE in the 460-650nm wavelength range, confirming the low contribution of the AlGaAs layer in the photocurrent. At shorter wavelengths (<390nm), on the contrary, this comparison shows that carriers photogenerated in the AlInP layer may contribute to the EQE. However, the low density of sunlight photons in this wavelength range results in a low impact in the overall efficiency. The colored region corresponds to the estimated contribution of carriers generated in the AlInP layer and accounts for an increase of the short-circuit current density of 0.1mA/cm^2.

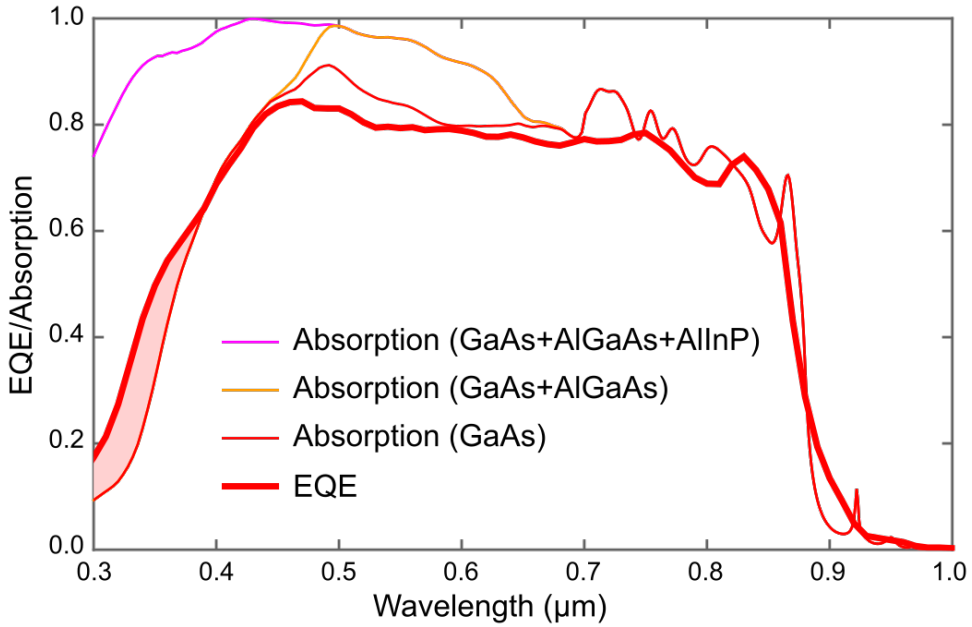

Supplementary Figure 8: Comparison of EQE measurement with optical simulations: absorption in the GaAs layer, in the GaAs and the AlGaAs BSF, or in the GaAs, AlGaAs and AlInP (window) layers for the solar cell with a nanostructured back mirror. The colored region at short wavelengths is attributed to contributions from the AlInP layer and amounts for 0.1mA/cm^2 to the total Jsc.

Supplementary Note 5: Theoretical limit for GaAs solar cells

Owning to the near optimal bandgap and its high external radiative efficiency, GaAs is the material of choice to reach the Shockley-Queisser (SQ) limit for photoconversion efficiency [2]. Photon recycling is recognized as an important factor toward the detailed balance limit of SQ [3]. When high-quality GaAs with internal radiative efficiency approaching 100% is available, the solar cell design should maximize the external luminescence yield [4]. We apply the detailed balance argument for ultrathin GaAs solar cells to derive the limiting efficiencies as a function of the active layer thickness *t*. We compare three structures:

- active layers on inactive GaAs substrate with perfect anti-reflection coating (ARC) leading to single-pass absorption (SPA): $A(E) = 1 - \exp(-\alpha(E)t)$
- active layers with a perfect back mirror and ARC leading to double-pass absorption (DPA): $A(E) = 1 - \exp(-2\alpha(E)t)$
- lambertian scattering (LS) with a perfect back mirror and ARC, which can be modeled by the approximate expression [5]: $A(E) = \frac{\alpha(E)t}{\alpha(E)t+1/4n^2}$

In Supplementary Figure 9(a), we can see that the short-circuit current decreases rapidly for GaAs thicknesses below 1 µm in the case of single-pass and double-pass absorption. In contrast, the lambertian scattering model suggests that the J_{sc} loss could be less than 10% for a thickness of 200 nm.

The balance between carrier generation, recombination and the photocurrent drawn from the solar cell can be written:

$$J/q = \int_0^\infty A(E)\times\phi_{AM1.5G}(E)dE - \frac{1}{\eta_{ext}}\exp\left(\frac{qV}{kT}\right)\int\int A(E,\theta)\times\phi_{bb}(E)\cos(\theta)\,d\Omega\,dE \quad \text{(Supplementary Equation 1)}$$

$$\phi_{bb}(E) = \frac{2}{h^3c^2}\times\frac{E^2}{\exp\left(\frac{E}{kT}\right)-1} \quad \text{(Supplementary Equation 2)}$$

where *q* is the elementary charge, *h* the Planck's constant, *c* the speed of light, k the Boltzmann constant and *T* the cell temperature. θ denotes the polar angle between incident or emitted light and surface normal, *E* the photon energy, $A(E,\theta)$ the absorption spectrum of the cell, $\phi_{AM1.5G}(E)$ the standard solar spectrum and $\phi_{bb}(E)$ the blackbody radiation. *J* is the current density extracted from the cell and *V* the bias voltage. The first term in the right-hand side of Supplementary Equation 1 is the photogenerated current, and the second term is the recombination current including the photon flux escape from the front surface and other losses via the definition for external luminescence efficiency η_{ext}. Absorption of incident light is supposed to be angular independent due to small solar disk (we consider normal incidence). As we can see in Supplementary Equation 1, the current-voltage characteristic of an ideal solar cell is entirelly determined by the absorptivity of the cell and the external luminescence efficiency.

In the case of a cell on an inactive substrate (SP absorption, blue curves in Supplementary Figure 9), we can see that the J_{sc} decreases rapidly for GaAs thicknesses below 1 µm (Supplementary Figure 9(a)). In Supplementary Figure 9(b), it is shown that the V_{oc} limit is penalized by the poor external luminescence efficiency due to pararistic absorption loss in the substrate. It is evaluated numerically according to reference [4] and results in $\eta_{ext} \approx 0.025$ for a GaAs thickness of *t*=205nm.

With perfect back mirrors (green curves and red curves in Supplementary Figure 9), no pararistic absorption or loss are considered: unity external yield is assumed ($\eta_{ext} = 1$). When compared to the flat mirror, lambertian scattering induces a significant increase of Jsc. However, the enhancement of near-bandgap absorption also increases light emission. It results in a decrease of the open-circuit voltage as compared to the flat mirror case, called an *effective photonic bandgap narrowing* (ΔVoc=40mV). This counterintuitive effect and the other optical factors impacting the Voc are detailed in references [4,6-8]. Overall, Supplementary Figure 9(c) shows that the efficiency limit of ultrathin solar cells is mainly due to the short-circuit current. For micrometer-thick layers, a back mirror has a minor effect on J_{sc}, but a great improvement on V_{oc} thanks to photon recycling.

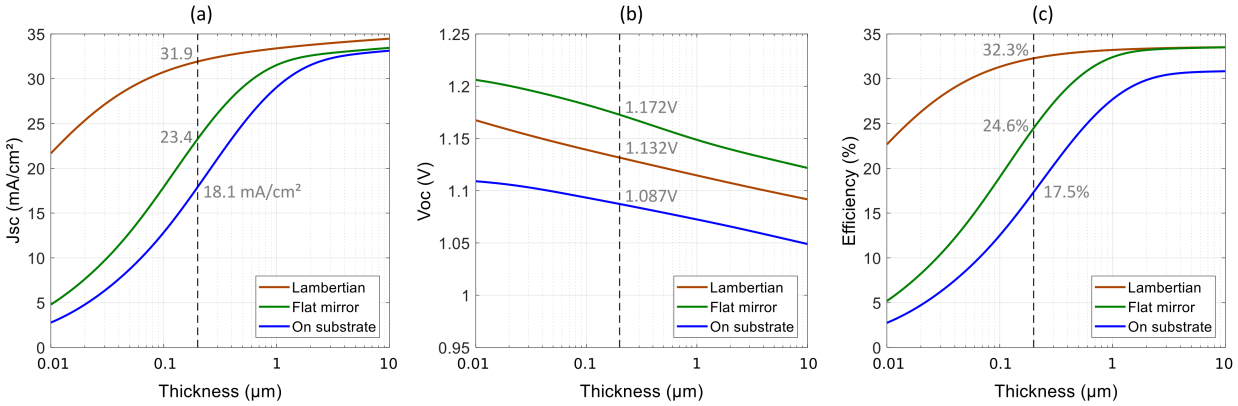

Supplementary Figure 9: Light-trapping models as functions of the GaAs absorber thickness (radiative limit): (a) Jsc, (b) Voc, (c) efficiency. Three models are considered: solar cells on an inactive substrate (blue, single-pass absorption), with a perfect back mirror (green, double-pass absorption) and with lambertian scattering (brown). The grey dashed vertical lines and values show the case of a 200 nm-thick GaAs absorber.

Fraunhofer ISE

Measurement report

4C2N-C2853a-B5-0917

Object:	GaAs cell
Manufacturer:	C2N
Serial Number:	C2853a-B5
Internal Serial Number:	C2853a-B5
Customer:	Centre for Nanoscience and Nanotechnology C2N, CNRS University Paris-Sud Paris-Saclay, 91120 Palaiseau, France
Datafile:	14276_C2853a-B5
Number of pages:	4
Date of calibration:	Sept. 14, 2017

Head of laboratory: Freiburg, May 28, 2019 Person in charge:

Gerald Siefer *Michael Schachtner*

Supplementary Figure 10: Measurement report by the Fraunhofer ISE CalLab. Spectral response, page 1/4.

1. Description of the calibrated object

The device under test (DUT) is a single junction GaAS solar cell on glass substrate. The electrical front side contacts is realized with Kelvin probes on the chip. The temporal stability of the solar cell performance was not determined.

2. Measurement procedure

The measurement of the relative spectral response on the solar cell was carried out with the DSR method /1/ on a grating monochromator setup according to /2/. The relative spectral responsivity was measured using a primary calibrated solar cell as a reference:

Traceability of the reference cells:

Identity-Nr.:	Certificate-Nr.:	Traceability:	
HamRef5-2017	47159-PTB-17	PTB	(280 - 1200 nm)
GePDRef1-2015	47032-PTB-15	PTB	(800 - 2000 nm)

The entire inspection equipment used is subject to a controlled quality management system according to ISO 9001:2000. All relevant components belonging to the filter monochromator setup external and respectively internal calibration certificates are available.

3. Measurement conditions

The terminal voltage of the solar cell is controlled by a current-to–voltage converter to 0V +/-3mV . The frequency of the chopped quasi monochromatic light beam is 181 Hz. The spectral bandwidth (full width at half maximum) of monochromatic light is below 10 nm.

Supplementary Figure 11: Measurement report by the Fraunhofer ISE CalLab. Spectral response, page 2/4.

4. Measurement result

Wavelength [nm]	norm. EQE [%]
280	0.12359
290	0.16556
300	0.20614
310	0.25265
320	0.32431
330	0.41986
340	0.51748
350	0.58963
360	0.64651
370	0.6835
380	0.72182
390	0.76178
400	0.81576
410	0.8578
420	0.89681
430	0.94093
440	0.97134
450	0.98883
460	0.99883
470	1
480	0.98852
490	0.98536
500	0.98714
510	0.97323
520	0.95416
530	0.94332
540	0.94172
550	0.94214
560	0.93989
570	0.9375
580	0.93512
590	0.93694
600	0.93586
610	0.93072
620	0.92182
630	0.92113
640	0.92775
650	0.9206
660	0.91195
670	0.90639
680	0.90172
690	0.91016
700	0.91748
710	0.91396
720	0.91357
730	0.91593
740	0.92815
750	0.93079
760	0.91134
770	0.89273
780	0.85976
790	0.83183
800	0.81867
810	0.81673
820	0.85958
830	0.8784
840	0.84767
850	0.80991
860	0.73788
870	0.51034
880	3.43E-01
890	0.23339
900	0.16081
910	0.11367
920	0.05967
930	0.03066
940	0.02575
950	0.02117
960	0.01697
970	0.00831
980	0.00459
990	0.00459
1000	0.00324
1010	0.00293
1020	0.00124

Supplementary Figure 12: Measurement report by the Fraunhofer ISE CalLab. Spectral response, page 3/4.

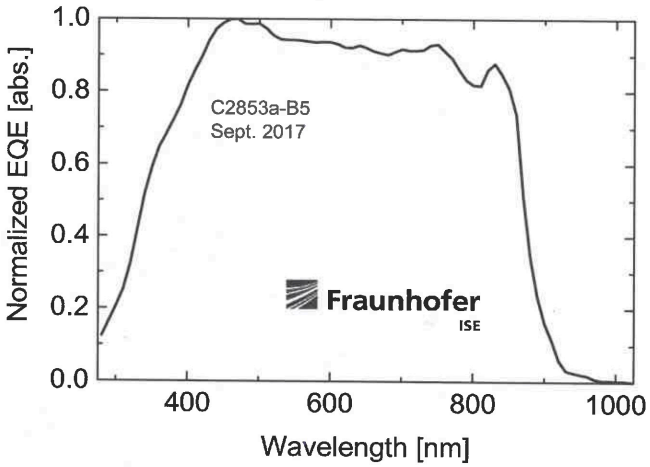

5. Literature

/1/ J. Metzdorf, Calibration of Solar Cells. 1: *The Differential Spectral Responsivity Method*, Applied Optics 26 (1987) p.1701-1708

/2/ IEC 60904-8:1998, Photovoltaic devices - Part 8: *Measurement of the spectral response of a photovoltaic (PV) device*

Supplementary Figure 13: Measurement report by the Fraunhofer ISE CalLab. Spectral response, page 4/4.

Fraunhofer ISE

Proprietary calibration report

1C2N-C2853a-B5-0917

Object:	GaAs cell
Manufacturer:	C2N
Serial number:	C2853a-B5
Internal serial number:	C2853a-B5
Customer:	Centre for Nanoscience and Nanotechnology C2N, CNRS University Paris-Sud Paris-Saclay, 91120 Palaiseau, France
Datafile:	08577_C2853a-B5
Number of pages:	5
Date of calibration:	Sept. 27, 2017

Head of laboratory: Freiburg, June 6, 2019 Person in charge:

Gerald Siefer *Michael Schachtner*

Supplementary Figure 14: Proprietary calibration report by the Fraunhofer ISE CalLab. IV measurements under Standard Testing Conditions (AM1.5G, 1000 W/m², 25°C), page 1/5.

1. Description of the calibrated object

The device under test (DUT) is a single junction GaAS solar cell on glass substrate. The electrical front side contacts is realized with Kelvin probes on the chip. The temporal stability of the solar cell performance was not determined.

2. Measurement procedure

The calibration of the test sample was performed at Standard Testing Conditions (STC) in accordance with /1/ under irradiation with a steady-state triple source solar simulator. The temperature is measured with a PT-100 surface sensor or determined by the V_{OC}-method /6/.

Traceability of the reference cell:

Identity-Nr.:	Certificate-Nr.:	Traceability:
TF31-2	47028-PTB-16	PTB

The spectral adjustment of the triple source simulator has been performed by a generalized mismatch correction /3/.

For the spectral adjustment of the triple source simulator, the spectral distribution of the individual light sources is measured with a spectroradiometer, the spectral response of the DUT is measured with a grating monochromator according to /4/ (see report 4C2N-C2853a-B5-0917).

The traceability of the measurement of the spectral distribution to World Radiation Scale is achieved using a standard-lamp for the calibration of the spectroradiometer.

Traceability of the standard lamp:

Identity-Nr.:	Certificate-Nr.:	Traceability
BN-9101-451	40006-17-PTB	PTB

The entire inspection equipment used is subject to a controlled quality management system according to ISO 9001:2000.

Supplementary Figure 15: Proprietary calibration report by the Fraunhofer ISE CalLab. IV measurements under Standard Testing Conditions (AM1.5G, 1000 W/m², 25°C), page 2/5.

3. Measurement conditions:

Standard Testing Conditions (STC):

Total Irradiance:	1000 W/m²
Temperature of the DUT:	25°C
Spectral irradiance distribution:	AM1.5G, IEC 60904-3, ed.2 /2/

The measurement of the IV-curve is performed with a 4-quadrant power amplifier.

4. Result of the measurement

Area [mm²]: (4.020 ± 0.020) (aperture area)

IV-curve parameter under standard testing conditions (STC):

V_{OC} [V]	=	(1.0223	± 0.0051)
I_{SC} [mA]	=	(0.991	± 0.019)
J_{SC} [mA/cm²]	=	(24.64	± 0.49)
I_{Mpp} [mA]	=	0.921	
V_{Mpp} [V]	=	0.8706	
P_{Mpp} [mW]	=	(0.802	± 0.019)
FF [%]	=	79.2	
η [%]	=	(19.9	± 0.50)

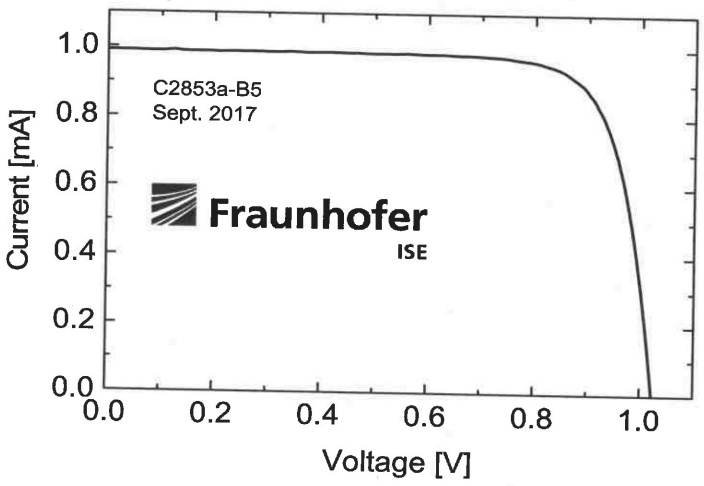

Supplementary Figure 16: Proprietary calibration report by the Fraunhofer ISE CalLab. IV measurements under Standard Testing Conditions (AM1.5G, 1000 W/m², 25°C), page 3/5.

Voltage [V]	Current [mA]
-0.05709	0.99284
-0.03981	0.99182
-0.0227	0.9906
-0.00529	0.98967
0.0137	0.99029
0.03148	0.98978
0.04975	0.98969
0.06742	0.98918
0.08551	0.98891
0.10385	0.98894
0.12349	0.99135
0.13931	0.98894
0.15659	0.98795
0.17502	0.98802
0.19311	0.98783
0.2107	0.98707
0.23021	0.98829
0.2484	0.98813
0.2666	0.98797
0.28508	0.98809
0.30258	0.98732
0.32105	0.98743
0.34076	0.98885
0.35781	0.98755
0.37515	0.98667
0.39381	0.98698
0.41284	0.98769
0.43099	0.98749
0.44788	0.98608
0.46697	0.98684
0.48371	0.98531
0.50191	0.98516
0.52043	0.98535
0.53856	0.98518
0.55832	0.98656
0.57517	0.98507
0.59235	0.98395
0.61047	0.98375
0.62881	0.9838
0.64595	0.9826
0.66324	0.98159
0.6815	0.9816
0.69816	0.97997
0.7152	0.97866
0.73219	0.97736
0.74706	0.97518
0.76174	0.97156
0.77713	0.96866
0.79261	0.96583
0.80677	0.96166
0.81927	0.9559
0.8321	0.95049
0.84382	0.94393
0.8546	0.93651
0.8635	0.92718
0.87213	0.9176
0.88072	0.90796
0.88929	0.89832
0.89618	0.88698
0.9018	0.87406
0.90828	0.86235

Voltage [V]	Current [mA]
0.91375	0.8496
0.91801	0.83572
0.92311	0.82264
0.92795	0.80931
0.932	0.79516
0.93557	0.78052
0.93956	0.76637
0.94318	0.75183
0.94627	0.73672
0.94936	0.72169
0.95235	0.70652
0.9556	0.69161
0.95816	0.67598
0.96076	0.66044
0.96338	0.64489
0.96574	0.62921
0.9681	0.61337
0.97028	0.59745
0.97244	0.58144
0.97454	0.56543
0.97649	0.55036
0.97853	0.53424
0.98023	0.5178
0.9822	0.50163
0.98391	0.48523
0.98565	0.46881
0.98739	0.45241
0.98906	0.43592
0.9906	0.41934
0.9922	0.40276
0.99377	0.38621
0.99515	0.36942
0.99664	0.35289
0.9981	0.33618
0.99957	0.31953
1.001	0.30277
1.00236	0.28597
1.00367	0.26911
1.00498	0.2523
1.00632	0.23546
1.00758	0.21866
1.00883	0.20174
1.01003	0.18482
1.01124	0.16785
1.01247	0.15095
1.01367	0.13402
1.01478	0.11701
1.01597	0.10005
1.01709	0.08304
1.01826	0.06614
1.01924	0.04899
1.02033	0.03192
1.02146	0.01487
1.02248	-0.00225
1.02356	-0.0193
1.02443	-0.03534
1.02546	-0.05248
1.02645	-0.06957
1.02747	-0.08672
1.02848	-0.10383
1.02946	-0.12098

Supplementary Figure 17: Proprietary calibration report by the Fraunhofer ISE CalLab. IV measurements under Standard Testing Conditions (AM1.5G, 1000 W/m², 25°C), page 4/5.

5.Literature:

/1/ IEC 60904-1: 1987, Photovoltaic devices - Part 1: Measurement of photovoltaic current-voltage characteristics

/2/ IEC 60904-3(ed2.): 2008 Photovoltaic Devices: Part 3. Measurement Principles for Terrestrial Photovoltaic (PV) Solar Devices with Reference Spectral Irradiance Data

/3/ IEC 60904-7: 1998, Photovoltaic devices - Part 7: Compution of the spectral mismatch error introduced in the testing of a photovoltaic device

/4/ M. Meusel, R. Adelhelm, F. Dimroth, A.W. Bett, W. Warta Spectral Mismatch Correction and Spectrometric Characterization of Monolithic III–V Multi-junction Solar Cells Prog. Photovolt: Res. Appl. 10 (2002) p. 243–255

/5/ IEC 60904-8: 1998, Photovoltaic devices - Part 8: Measurement of the spectral response of a photovoltaic (PV) device

/5/ IEC 60904-9: 1995, Photovoltaic devices - Part 9: Solar simulator performance requirements

/6/ K. Emery et al, Temperature dependence of photovoltaic cells, modules and systems, Proceedings of the 25th IEEE Photovoltaic Specialists Conference, Washington DC, USA, p. 1275-1278

Supplementary Figure 18: Proprietary calibration report by the Fraunhofer ISE CalLab. IV measurements under Standard Testing Conditions (AM1.5G, 1000 W/m², 25°C), page 5/5.

Supplementary References

[1] Yeh, P. Optical waves in layered media (New York : Wiley) (1988).

[2] Shockley, W., and Queisser, H. J. Detailed Balance Limit of Efficiency of p-n Junction Solar Cells. *Journal of Applied Physics* **32**, 510–519 (1961).

[3] Martí, A., Balenzategui, J. L., and Reyna, R. F. Photon recycling and Shockley's diode equation. *Journal of Applied Physics* **82**, 4067–4075 (1997).

[4] Miller, O. D., Yablonovitch, E., and Kurtz, S.R. Strong Internal and External Luminescence as Solar Cells Approach the Shockley-Queisser Limit. *IEEE Journal of Photovoltaics* **2**, 303–311 (2012).

[5] Green, M. A. Lambertian light trapping in textured solar cells and light-emitting diodes: analytical solutions. *Prog. in Photovolt: Res. Appl.* **10**, 235–241 (2002).

[6] Ganapati, V., Steiner, M. A., and Yablonovitch, E. The Voltage Boost Enabled by Luminescence Extraction in Solar Cells. *IEEE Journal of Photovoltaics* **6**, 801–809 (2016).

[7] Munday, J. N. The effect of photonic bandgap materials on the Shockley-Queisser limit. *Journal of Applied Physics* **112**, 064501 (2012).

[8] Rau, U., Paetzold, U. W., and Kirchartz, T. Thermodynamics of light management in photovoltaic devices. *Phys. Rev. B* **90**, 035211 (2014).